# Effects Caused by Varying the Strength of the Capping Inversion Based on a Large Eddy Simulation Model of the Shear-Free Convective Boundary Layer

ZBIGNIEW SORBJAN

*School of Meteorology, University of Oklahoma, Norman, Oklahoma*

(Manuscript received 14 June 1995, in final form 25 January 1996)

ABSTRACT

Effects caused by variation of the potential temperature lapse rate $\Gamma$ in the free atmosphere are examined based on a "large eddy simulation" model of the shear-free convective atmospheric boundary layer. The obtained results show that only near the top of the boundary layer are the statistical moments involving temperature strongly sensitive to changes of the parameter $\Gamma$. Furthermore, the moments involving only the vertical velocity are practically independent of $\Gamma$. The ratio $R$ of the heat fluxes at the top and the bottom of the mixed layer increases when $\Gamma$ increases. For the values of $\Gamma$ from 1 to 10 K/km, typically observed in the atmosphere, the heat flux ratio $R$ varies in the range $-0.2$ to $-0.3$. When $\Gamma$ increases by an order of magnitude to 100 K/km, $R$ increases only slightly to about $-0.4$. When $\Gamma$ decreases to zero, the heat flux $H_i$ at the top of the mixed layer also decreases to zero. In this case, the thermal structure of the atmospheric boundary layer is found to be similar to nonpenetrative "solid lid" convection in a tank.

## 1. Introduction

Convection in the atmospheric boundary layer is inherently associated with entrainment of mass, heat, and momentum from the capping temperature inversion. Entrainment is caused by updrafts that penetrate the stably stratified layer above the mixed layer and induce a compensating downflow of relatively warmer air. Effects of entrainment are important to the dynamics of the mixed layer and have been studied experimentally and numerically in the past (e.g., Deardorff et al. 1969; Deardorff 1974b; Willis and Deardorff 1974; Caughey and Palmer 1979; Deardorff et al. 1980; Adrian et al. 1986; Kumar and Adrian 1986). Numerous parameterization schemes have been proposed based on these investigations (e.g., Lilly 1968; Zeman and Tennekes 1977; Mahrt 1979; Boers 1989).

Atmospheric convection is often referred to as penetrative convection. Another form of convective regime—nonpenetrative convection—is also possible in nature (e.g., Adrian et al. 1986). The basic difference between both cases is that in nonpenetrative convection updrafts cannot overshoot above the height of the mixed layer. As a result, the heat flux on the top of the mixed layer vanishes. Despite the fact that nonpenetrative convection is entrainment-free, there exists an intriguing resemblance of some of its statistics to analogous statistics of penetrative convection. This resemblance is exhibited by various dimensionless moments involving temperature in the lower portion of the mixed layer. Near the top of the mixed layer, similarity disappears due to effects of entrainment and gravity waves.

Nonpenetrative convection with a solid lid on the top of the vertical domain was studied in a tank by Adrian et al. (1986). The same type of convection was also simulated numerically by Krettenauer and Schumann (1992) and Sorbjan (1996). Sorbjan observed that nonpenetrative convection was organized into separate columns of updrafts and downdrafts extending from the bottom to the top of the domain. Temperature and humidity fields in nonpenetrative regimes were perfectly correlated. Sorbjan (1990) showed that nonpenetrative convection is self-similar with convective scales proposed by Deardorff (1970a,b).

Intuitively, nonpenetrative convection in the atmosphere could be considered as a "limit case" when the heat flux at the top of the mixed layer vanishes. One could argue that this limit case would occur if there were an infinitely large temperature lapse rate at the top of the atmospheric mixed layer. In this case, a huge negative buoyancy force in an extremely strong inversion layer above the mixed layer would have an effect analogous to a solid lid in a tank. The basic goal of this paper is to study such a limit case by examining conditions that would allow entrainment-free convection in the atmosphere. For this purpose, results produced by a large eddy simulation model of Sorbjan (1996) are analyzed. The model runs are designed to investigate the effects of variation of the temperature lapse

*Corresponding author address:* Dr. Zbigniew Sorbjan, School of Meteorology, University of Oklahoma, Energy Center, Room 1310, 100 E. Boyd Street, Norman, OK 73019-0470.
E-mail: zsorbjan@uoknor.edu

© 1996 American Meteorological Society

Unauthenticated | Downloaded 10/24/21 10:51 AM UTC

TABLE 1. Characteristics of performed simulations.

| Run | Time steps | Space domain | $\Delta t$ [s] | $\Delta x$ [m] | $\Delta z$ [m] | $w^*$ [m s$^{-1}$] | $T^*$ [K] | $\Gamma$ [K/km] | $z_i$ [m] | $-z_i/L$ | $t^*$ [s] | $S = Nt^*$ |
|---|---|---|---|---|---|---|---|---|---|---|---|---|
| P1 | 6000 | $32^2 \times 55$ | 2.5 | 100 | 20 | 0.269 | 0.0037 | 1 | 590 | 165.2 | 2193 | 12.7 |
| P2 | 6000 | $32^2 \times 55$ | 2.5 | 100 | 20 | 0.256 | 0.0039 | 10 | 510 | 163.6 | 1992 | 35.5 |
| P3 | 6000 | $32^2 \times 55$ | 2.5 | 100 | 20 | 0.252 | 0.0040 | 100 | 490 | 144.4 | 1944 | 112.4 |
| P4 | 6000 | $32^2 \times 55$ | 2.5 | 100 | 20 | 0.262 | 0.0038 | 3 | 550 | 161.2 | 2099 | 21.0 |
| N1 | 6000 | $32^2 \times 100$ | 3.0 | 100 | 35 | 0.409 | 0.0024 | 0.01 | 2082 | 340.1 | 5090 | 2.9 |
| N2 | 12 000 | $32^2 \times 60$ | 5.0 | 200 | 100 | 0.502 | 0.0020 | 0.01 | 3850 | 472.8 | 7669 | 4.4 |

rate in the "capping" inversion layer. Contrary to the numerical simulation of Sorbjan (1996), the "solid lid" constraint on the top of the mixed layer was not applied in this study.

The obtained results are presented in sections 2, 3, and 4. Section 2 briefly introduces the large eddy simulation model and also summarizes the performed numerical simulations. In section 3, the effects of variation of the inversion strength are discussed. Section 4 presents results of the numerical simulations for the case when the potential temperature lapse rate at the top of the mixed layer vanishes.

## 2. Numerical simulations

A detailed description of the large-eddy simulation (LES) model used in this study is presented by Sorbjan (1996). The model employs a system of six differential equations consisting of conservation laws for momentum, mass, and the first law of thermodynamics. The unknown quantities include three components of velocity, virtual potential temperature, specific humidity, and pressure. The adopted subgrid parameterization is based on the kinetic energy equation and follows the scheme developed by Schumann (1991a,b).

Horizontal boundary conditions are assumed to be periodic. At the lower boundary, the vertical derivative of the turbulent kinetic energy is set to zero. The Monin–Obukhov similarity formulation is employed to calculate surface momentum fluxes (e.g., Schmidt and Schumann 1989). The surface temperature and humidity fluxes $H_0$ and $Q_0$ are prescribed. The upper boundary condition is assumed to be stress free for horizontal velocity components. The vertical velocity is set to zero at the top of the computational domain (no subsidence assumed), the potential temperature lapse rate $\Gamma$ is specified, a lapse rate for humidity is nil, and a zero turbulent kinetic energy is assumed.

The model was run for a number of time steps with constant fluxes of surface temperature and humidity, $H_0 = 0.001$ K m s$^{-1}$, and $Q_0 = 0.005$ g kg$^{-1}$ m s$^{-1}$. Initially, the atmosphere was assumed to be at rest. The initial potential temperature profile was constant (=300 K) with height within the mixed layer that was 500 m deep. Above the mixed layer, the potential temperature increased with a constant positive lapse rate $\Gamma$. The initial potential humidity profile was constant (=1 g kg$^{-1}$) with height within the mixed layer and zero above. The geostrophic wind was assumed to be zero. The roughness length was $z_0 = 0.16$ m.

The numerical characteristics of the performed simulations are presented in Table 1. Symbols $\Delta t$, $\Delta x = \Delta y$, and $\Delta z$ indicate time and space increments; $w^* = (\beta z_i H_0)^{1/3}$, $T^* = H_0/w^*$, and $q^* = Q_0/w^*$ are the convective scales for vertical velocity, temperature, and humidity, respectively; $z_i$ is the mixed layer height (level of the minimum heat flux); $\beta = g/T_0$ is the buoyancy parameter; $g$ is the gravity acceleration; $T_0$ is a reference potential temperature; $t^* = z_i/w^*$ is the convective timescale; $\Gamma$ is the virtual potential temperature lapse rate in the free atmosphere; $L$ is the Monin–Obukhov length, and $N = (\beta\Gamma)^{0.5}$ is the Brunt–Väisälä frequency; and $S = Nt^*$ is the inverse Froude number.

Runs P1–P4 were simulated for different values of the potential temperature lapse rates $\Gamma$, varying from 1 to 100 K/km. In the real atmosphere, the potential temperature lapse rate depends on latitude and on season. Its global mean rate is about 3.5 K/km. The typical middle latitude values are in the range 1–3 K/km in winter, and 4–5 K/km in summer (e.g., Hartman 1994). The unrealistic value of $\Gamma = 100$ K/km in run P3 was used to examine the impact of an extremely strong capping inversion. Runs N1 and N2 were simulated for a very small value of the temperature lapse rate, 0.01 K/km.

Time integrations for runs P1–P4 were performed over a period ranging from 6.8 to 7.7 convective timescales $t^*$. The relative size of horizontal domains ranged from $5.4–6.5z_i$. During runs N1 and N2, the mixed layer height $z_i$, and consequently the timescale $t^* = z_i/w^*$, was rapidly increasing. As a result, runs N1 and N2 were performed in relatively shorter time intervals of 3.5 and $2.3t^*$. Also, their relative horizontal domains were reduced to about 1.5 and $1.7z_i$, respectively.

The results of all simulations were averaged in time and also horizontally in space. The time averaging for all runs P and for run N1 was performed every 25 time steps between 5500 and 6000 time steps. The time averaging for run N2 was executed every 50 time steps during the last 1000 time steps. Large values of the parameter $-z_i/L$ during all simulations indicate ex-

Unauthenticated | Downloaded 10/24/21 10:51 AM UTC

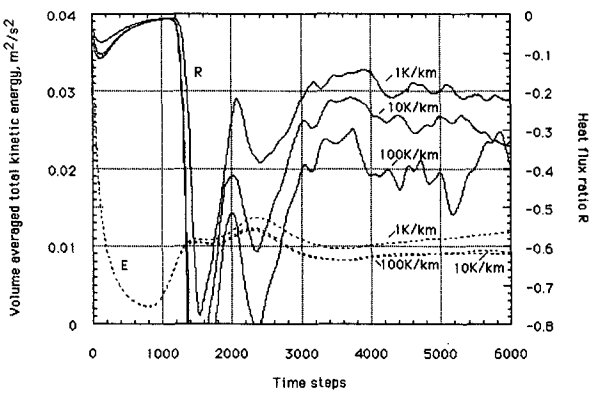


FIG. 1. Time history of the volume-averaged total kinetic energy $E$ (dotted lines) and of the heat flux ratio $R$ (solid lines) for simulations P1 ($\Gamma$ = 1 K/km), P2 ($\Gamma$ = 10 K/km), and P3 ($\Gamma$ = 100 K/km).

tremely convective conditions even though $H_0$ is quite small.

## 3. Penetrative convection

### a. *Effects of* $\Gamma$ *variations*

In order to examine the effects caused by changes in the potential temperature lapse rate at the top of the atmospheric mixed layer, we simulated three cases: P1, P2, and P3. The time history plot for these three simulations is depicted in Fig. 1. The figure displays two characteristics of turbulence: the total (subgrid plus resolvable), volume-averaged (in the entire computational domain) kinetic energy $E$, and also the heat flux ratio $R = H_i/H_0$, where $H_i$ and $H_0$ are the heat fluxes at the top and the bottom of the mixed layer. The initial value of the volume-averaged kinetic energy is quite large (in order to cause intensive initial mixing), and it decreases with time due to the dissipation. Both the total kinetic energy and the heat flux ratio $R$ become steady-state after about 4000 time steps.

Figure 1 implies that the heat flux ratio $R$ is a variable dependent on $\Gamma$. The ratio $R$ increases when $\Gamma$ increases. For the values of $\Gamma$ from 1 to 10 K/km, typically observed in the atmosphere, the heat flux ratio $R$ varies in the range $-0.2$ to $-0.3$. This result agrees with atmospheric observations (e.g., Rayment and Readings 1974; Caughey 1982). When $\Gamma$ increases by an order of magnitude to 100 K/km, $R$ increases only slightly to about $-0.4$. This suggests that $R$ is not very sensitive to the variation of the lapse rate $\Gamma$ (for large $\Gamma$). This conclusion can be explained by considering the simplified temperature flux and temperature variance equations in which only the production and the dissipation terms are retained (Sorbjan 1990):

$$\overline{w'\theta'} = -\tau\left(\overline{w'^2}\frac{\partial\Theta}{\partial z} - \beta\overline{\theta'^2}\right) \tag{1a}$$

$$\frac{\overline{\theta'^2}}{\tau} = -\overline{w'\theta'}\frac{\partial\Theta}{\partial z}, \tag{1b}$$

where $\tau$ is the timescale. Equations (1a) and (1b) imply that both moments and $\overline{\theta'^2}$ depend locally on the temperature lapse rate $\partial\Theta/\partial z$. There is a negative contribution to $\overline{w'\theta}$ in Eq. (1) directly proportional to $d\Theta/dz$. But there is also a positive contribution proportional to $\overline{\theta'^2}$ which limits the value of $\overline{w'\theta}$, if $\partial\Theta/\partial z$ increases. Combining Eqs. (1a) and (1b) yields

$$\overline{w'\theta'} = -\frac{\tau\overline{w'^2}\dfrac{\partial\Theta}{\partial z}}{1 + \beta\tau^2\dfrac{\partial\Theta}{\partial z}}. \tag{2}$$

In the limit of large temperature lapse rate, $\overline{w'\theta'} \to -\epsilon/\beta$, where we assumed that the dissipation rate $\epsilon = \overline{w'^2}/\tau$. Assuming further that $\epsilon$ = const $w^{*3}/z_i$, we conclude that, indeed, in the limit of large $\Gamma$ the ratio $R$ should converge to a constant.

A further understanding on effects caused by variation of the parameter $\Gamma$ can be obtained by analyzing characteristics of conditionally averaged updrafts and downdrafts shown in Figs. 2 and 3. Updrafts are identified by positive vertical velocities. The mean potential temperature excess in updraft is defined as $\langle\theta'\rangle = \langle\theta^{\uparrow} - \{\theta\}\rangle$, where $\langle\cdot\rangle = [\{\cdot\}]$ is the time–space averaging operator, $[\cdot]$ indicates a time average, and $\{\cdot\}$ is a horizontal average. The mean vertical velocity in updrafts is defined as $\langle w'\rangle = \langle w^{\uparrow}\rangle$ (note that $\{w\} = 0$). Characteristics of downdrafts are defined analogously.

The mean vertical velocities and temperature excesses in updrafts and downdrafts in runs P1–P3 are shown in Figs. 2 and 3. The curves obtained in run P1 agree with atmospheric observations of Young (1988) as well as numerical simulations of Schumann and Moeng (1991) and Nieuwstadt et al. (1992). Figure 2

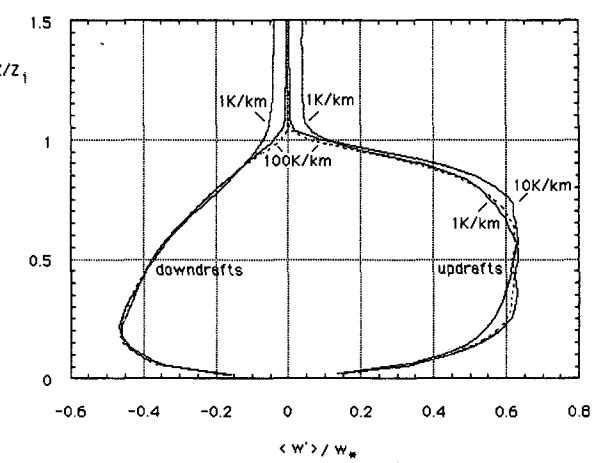


FIG. 2. Vertical velocity in updrafts and downdrafts for simulations P1 ($\Gamma$ = 1 K/km), P2 ($\Gamma$ = 10 K/km), and P3 ($\Gamma$ = 100 K/km).

Unauthenticated | Downloaded 10/24/21 10:51 AM UTC

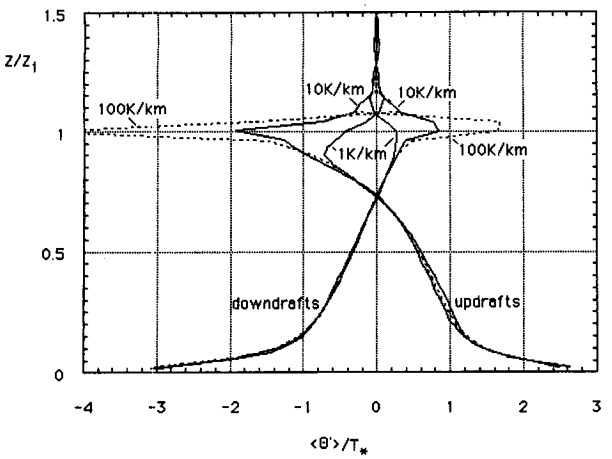


FIG. 3. Temperature excess in updrafts and downdrafts for simulations P1 ($\Gamma$ = 1 K/km), P2 ($\Gamma$ = 10 K/km), and P3 ($\Gamma$ = 100 K/km).

indicates that within the mixed layer the mean vertical velocities in both updrafts and downdrafts are practically independent of $\Gamma$. At the top of the mixed layer, the vertical velocity in updrafts is about $0.1w^*$. Above the mixed layer, the mean vertical velocity in updrafts and downdrafts is significantly reduced for larger values of $\Gamma$. Both Figs. 2 and 3 show that penetration of the inversion layer occurs (as indicated by positive velocity in updrafts) even though the updrafts are on average negatively buoyant ($\theta' < 0$). This agrees with tank observations of Kumar and Adrian (1986).

Even such an extremely large temperature lapse rate as 100 K/km does not completely prevent updrafts from penetrating the inversion layer. The larger values of $\Gamma$, the smaller the vertical velocity in updrafts is (Fig. 2), but at the same time, the hotter air is entrained into the mixed layer (Fig. 3). Consequently, when $\Gamma$ increases, the heat flux at the top of the mixed layer does not decrease, as might have been expected.

The humidity flux in runs P2–P4 is shown in Fig. 4. In run P1, the steady state for humidity was not reached within 6000 time steps, and therefore this case is not shown in Fig. 4. Since the capping inversion layer is dry, the humidity flux at the top of the mixed layer is positive. The figure indicates that $\Gamma$ has an opposite effect on the humidity flux than on the heat flux; that is, the humidity flux at the top of the mixed layer decreases when $\Gamma$ increases. This can be explained by the fact that the greater values of $\Gamma$, the weaker is the penetration of the stable layer.

### b. *Mixed layer statistics*

Mixed layer similarity assumes that in shearless dry convection various statistics of turbulence can be scaled using four convective scales: $w^*$, $T^*$, $q^*$, and $z_i$ for velocity, temperature, humidity, and height (Deardorff 1970a,b). If the parameter $\Gamma$ is excluded from the list of similarity parameters, dimensionless statistical moments in the mixed layer should be functions of only one dimensionless parameter, $z/z_i$. However, if the parameter $\Gamma$ is included, similarity functions should depend on the dimensionless height $z/z_i$ and also on another dimensionless parameter involving $\Gamma$, for instance a dimensionless parameter $S = t^*N$ listed in Table 1.

In order to understand the role of the temperature lapse rate $\Gamma$ as a potential similarity parameter, we analyzed various dimensionless moments involving vertical velocity, temperature, and humidity. Before presenting the obtained results, let us again inspect Figs. 2 and 3. Figure 2 shows that the vertical velocity in updrafts and in downdrafts is practically independent of $\Gamma$. Figure 3 indicates that the potential temperature in updrafts and also in downdrafts is dependent on $\Gamma$ in the layer $0.75-1.2z_i$. Based on these two figures, one could expect that, in general, near the inversion layer statistical moments involving temperature should have strong dependence on the parameter $\Gamma$. Moments that involve the vertical velocity alone should be nearly independent of $\Gamma$. Dependence on $\Gamma$ should increase for higher-order moments involving temperature. To examine this rule, we shall consider moments obtained for runs P1 and P2 in Figs. 5–11. Because some (not all) moments obtained for $\Gamma$ = 100 K/km have small, but sharp, ripples near the inversion layer (due to dispersion truncations errors at a sharp inversion), we do not display the moments generated during run P3 in Figs. 5–11.

Figure 5 depicts the dimensionless temperature lapse rate obtained for $\Gamma$ = 1 and 10 K/km. The figure shows that in the layer $0 < z/z_i < 0.9$ the dimensionless temperature lapse rate is independent of $\Gamma$. It strongly depends on $\Gamma$ above $z/z_i = 0.9$. The dimensionless tem-

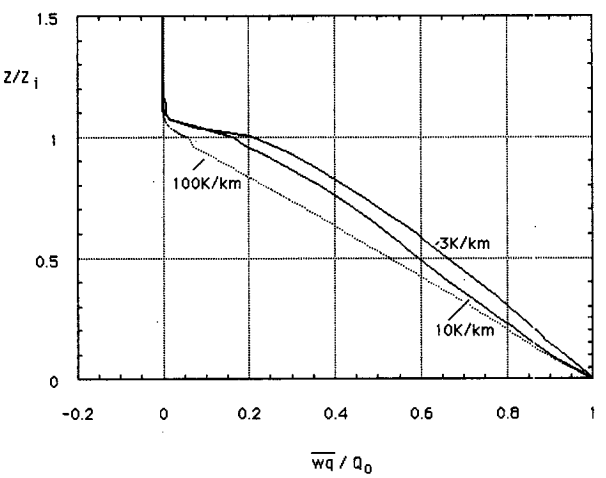


FIG. 4. Dimensionless specific humidity flux for simulations P2 ($\Gamma$ = 10 K/km), P3 ($\Gamma$ = 100 K/km), and P4 ($\Gamma$ = 3 K/km).

Unauthenticated | Downloaded 10/24/21 10:51 AM UTC

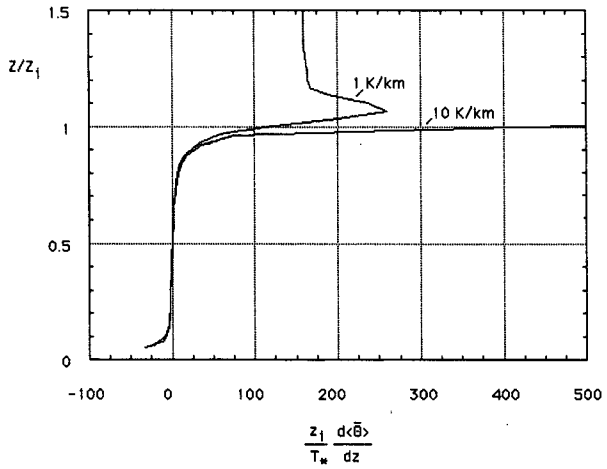


FIG. 5. Dimensionless lapse rate of the virtual potential temperature for simulations P1 ($\Gamma$ = 1 K/km) and P2 ($\Gamma$ = 10 K/km).

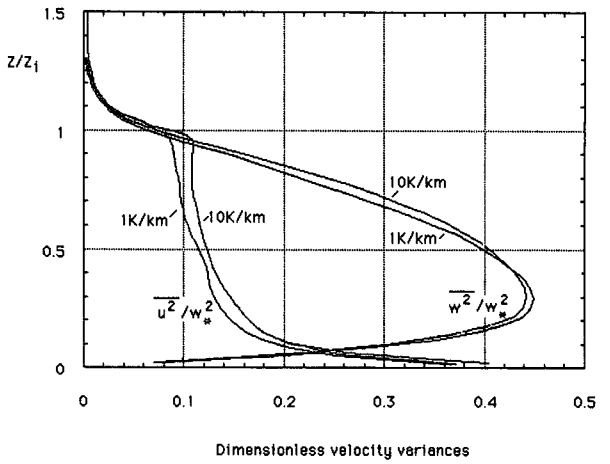


FIG. 7. Dimensionless horizontal and vertical velocity variances (scaled by $w^{*2}$) for simulations P1 ($\Gamma$ = 1 K/km) and P2 ($\Gamma$ = 10 K/km).

perature lapse rate has a peak at $z/z_i = 1.1$. The peak is caused by the cooling by updrafts that takes place in the interfacial layer above the mixed layer (e.g., Sorbjan 1995). Because values of the dimensionless temperature lapse rates in runs P1 and P2 change sign and vary over three orders of magnitude, a full profile is shown only for run P1. The peak values of the dimensionless temperature lapse rate are about 250 for P1 and 1689 for P2.

The dimensionless total variance for virtual potential temperature is presented in Fig. 6. The total temperature variance is defined as $\sigma_\theta^2 = \langle \theta'^2 \rangle$ + SGC, where the subgrid component of the total variance is defined as SGC = $5\langle H_3 \rangle^2 / \langle E \rangle$, where $\langle H_3 \rangle$ is the averaged subgrid vertical temperature flux and $\langle E \rangle$ is the averaged subgrid turbulent kinetic energy (e.g., Nieuwstadt et al. 1992). The figure shows that in the layer $0 < z/z_i < 0.9$ the moment is independent of $\Gamma$. This finding disagrees with Wyngaard's (1985) predictions, which are independent of $R$ (and consequently on $\Gamma$) in a more shallow layer, $0 < z/z_i < 0.4$.

The variance reaches maximum for $z/z_i = 1.1$. The maximum is associated with the strength of the capping inversion and with development of gravity waves excited by penetrative convection. The magnitude of the maximum increases with increased $\Gamma$, in accord with results obtained previously by Deardorff (1974b).

The dimensionless total variances for the horizontal and vertical velocity components are presented in Fig. 7. The total velocity variance is defined as $\sigma_i^2 = \langle u_i'^2 \rangle$ + SGC, where the subgrid component SGC = $2/3\langle E \rangle$. As expected, the dimensionless vertical ve-

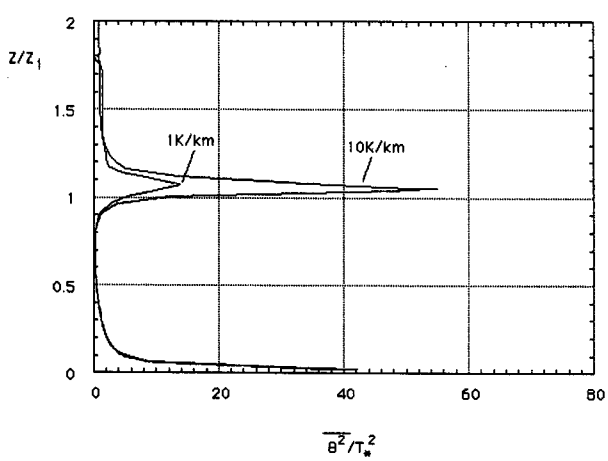


FIG. 6. Dimensionless variance of the virtual potential temperature for simulations P1 ($\Gamma$ = 1 K/km) and P2 ($\Gamma$ = 10 K/km).

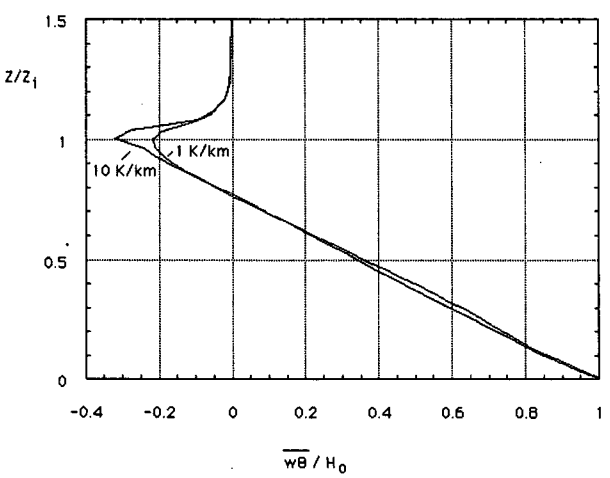


FIG. 8. Dimensionless virtual potential temperature flux for simulations P1 ($\Gamma$ = 1 K/km) and P2 ($\Gamma$ = 10 K/km).

Unauthenticated | Downloaded 10/24/21 10:51 AM UTC

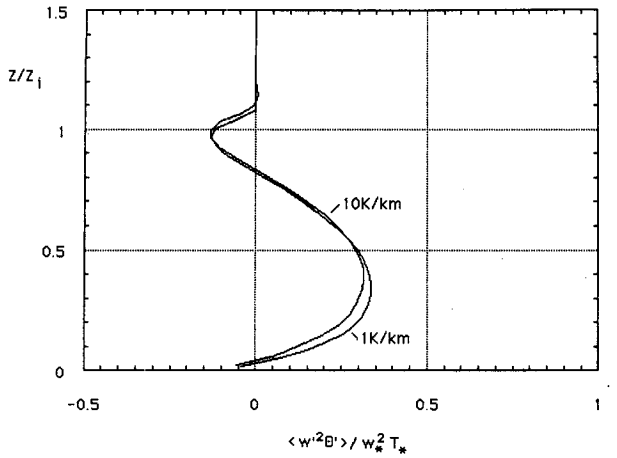


FIG. 9. Dimensionless vertical transport of the temperature flux for simulations P1 ($\Gamma$ = 1 K/km) and P2 ($\Gamma$ = 10 K/km).

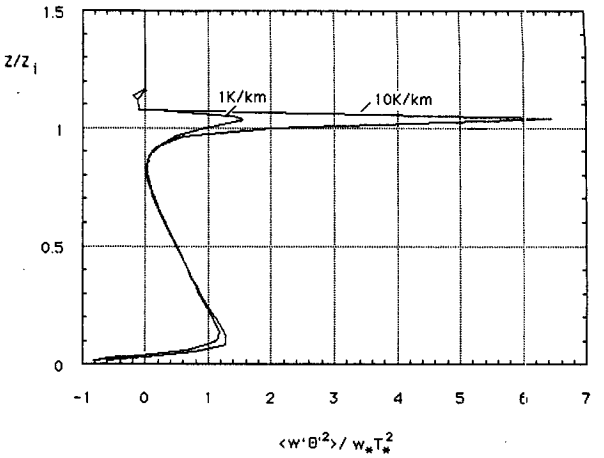


FIG. 10. Dimensionless vertical transport of the temperature variance for simulations P1 ($\Gamma$ = 1 K/km) and P2 ($\Gamma$ = 10 K/km).

locity variance in Fig. 7 is practically independent of $\Gamma$. The dimensionless horizontal velocity variance increases slightly with increasing $\Gamma$, especially near the top of the mixed layer.

The covariance of virtual potential temperature and vertical velocity (temperature flux) is shown in Fig. 8. The covariance is linear within the mixed layer and exhibits a weak dependence on the parameter $\Gamma$ near the top of the mixed layer (as previously seen in Fig. 1). The covariance reaches maximum at level $z_i$, defined as the mixed layer height. The top of the convective boundary layer could be defined as a level $h$, where the temperature flux vanishes. Figure 8 shows that $h \approx 1.2z_i$.

We expect that the third-order moment $\langle w'^2\theta' \rangle$ should be weakly dependent on $\Gamma$, while $\langle w'\theta'^2 \rangle$ should strongly vary when the parameter $\Gamma$ changes. These expectations are confirmed in Figs. 9 and 10. The peak values of the moments are reached at about $z = z_i$ for $\langle w'^2\theta' \rangle$ and at about $z = 1.05z_i$ for $\langle w'\theta'^2 \rangle$.

The moments of temperature and velocity presented above can be compared with tank observations of Kumar and Adrian (1986). Their experiments were performed for the dimensionless temperature lapse rates $\Gamma z_i/T^*$ in the range from 104.7 to 370.5. In comparison, the values of the dimensionless temperature lapse rate used in this study are larger: 159.5 for run P1, 1307.7 for P2, and 12 250 for run P3. Kumar and Adrian reported that $\Gamma$ has little effect on statistics in the mixed layer, which agrees with our results. Because the temperature lapse rates chosen by Kumar and Adrian were in a smaller range of values, their results are inconclusive regarding the dependence of the statistical moments on $\Gamma$ in the interfacial layer. Nevertheless, the statistics of velocity components and temperature presented by Kumar and Adrian agree favorably with our results from run P1 in Figs. 5–10. For instance, the dimensionless variances obtained by Kumar and Adrian at $z/z_i = 1$ were $\sigma_u^2/w^{*2} \sim 0.09$, $\sigma_w^2/w^{*2} \sim 0.09$, and $\sigma_\theta^2/\theta^{*2} \sim 9 - 16$.

Inspection of Figs. 5–10 shows that moments involving only vertical velocity components are practically independent of $\Gamma$. Moments that involve temperature (such as temperature lapse rate, temperature variance, and vertical transport of temperature variance) are independent of the parameter $\Gamma$, but only in the lower 90% of the mixed layer. In the layer ranging from $0.9z_i$ to $h \approx 1.2z_i$, statistics involving temperature depend on height $z$ and on the temperature lapse rate $\Gamma$. It is not clear if the regime in this layer is self-similar.

Figure 11 depicts the dimensionless variance for specific humidity. The figure shows that in the mixed layer, as well as in the interfacial layer above, the variance strongly depends on $\Gamma$. Contrary to the temperature variance, the humidity variance decreases when $\Gamma$ increases. This is due to the fact that the greater the values

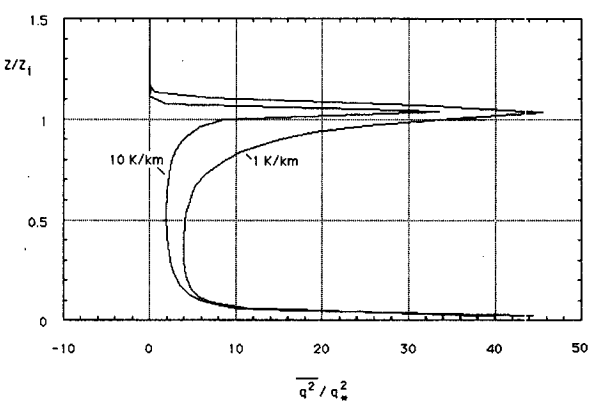


FIG. 11. Dimensionless variance of the specific humidity for simulations P1 ($\Gamma$ = 1 K/km) and P2 ($\Gamma$ = 10 K/km).

Unauthenticated | Downloaded 10/24/21 10:51 AM UTC

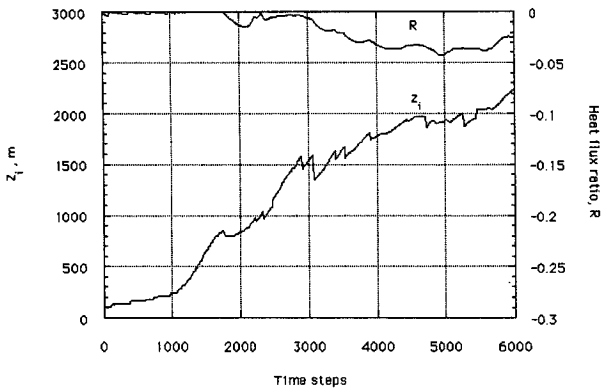


FIG. 12. Time history of the mixed layer height $z_i$ and of the heat flux ratio $R$ for simulation N1.

of $\Gamma$, the weaker is the penetration of the stable layer and the smaller is the amount of moisture air transported out of and dry air transported into the mixed layer. The humidity variance reaches maximum for $z/z_i = 1.05$.

## 4. Free encroachment

In the previous section we discussed the impact of the increasing values of the temperature lapse rate $\Gamma$ on the dynamics of the mixed layer. In this section, we will examine the case when $\Gamma$ is extremely small. A similar case was earlier considered by Deardorff (1974a) and Deardorff et al. (1980).

Let us first recall Eq. (2). The equation implies that when the lapse rate at the top of the mixed layer vanishes, the heat flux should also tend to zero. An identical conclusion can be reached based on Lilly's (1968) approximation of the heat flux at the top of the mixed layer:

$$H_i = -\Delta\theta\left(\frac{dz_i}{dt} - w_s\right), \qquad (3)$$

where $\Delta\theta$ is the temperature "jump" at the top of the mixed layer and $w_s$ is the large-scale subsidence velocity. The subsidence is assumed zero in this study. The above equation indicates that $H_i$ will vanish only in the case of "encroachment" (e.g., Carson and Smith 1974), when $\Delta\theta \equiv 0$. The latter requirement ($\Delta\theta \equiv 0$), however, can be achieved only when $\Gamma = 0$. If we assumed that initially $\Delta\theta = 0$ but $\Gamma \neq 0$, the heating and growing of the mixed layer would result in nonzero values of $\Delta\theta$. Consequently, $H_i$ would no longer be zero.

The considered case could be termed "free encroachment" (as the form of encroachment for which $\Gamma = 0$). Deardorff (1976) called this state the free entrainment. He also found that in this case the mixed layer growth represents the fastest possible rate, equal to $dz_i/dt = 0.2w^*$ (Deardorff 1974a).

Equation (3) indicates that $H_i$ could also vanish if $dz_i/dt = 0$ (provided $w_s = 0$). This case is equivalent to a "solid lid" nonpenetrative convection in a tank considered by Sorbjan (1996). As discussed in section 3a, the solid-lid state with $dz_i/dt = 0$ cannot be achieved in the atmospheric mixed layer with no subsidence, even for large $\Gamma$.

In order to verify an impact of a very small temperature lapse rate $\Gamma$, we simulated two runs: N1 and N2. As can be seen in Table 1, both runs were executed for $\Gamma = 0.01$ K/km. Runs N1 and N2 differ in the length of the simulation and in values of time and space increments. The time history of the heat flux ratio $R$ and the mixed layer height $z_i$ for run N1 is shown in Fig. 12. The heat flux ratio $R$ for N1 is about $-0.04$. This confirms our expectation that $R$ decreases with decreasing $\Gamma$ and approaches zero when $\Gamma \to 0$. The average growth rate of the mixed layer height between 3000 and 6000 time steps is quite rapid and equal to about $dz_i/dt = 600$ m/9000 s $= 240$ m/h. For $w^* = 0.409$ (Table 1), this gives $dz_i/dt = 0.16w^*$, quite close to Deardorff's (1974a) result.

In Fig. 13, the dimensionless total temperature heat fluxes are shown for runs N1, N2, and for run P4. Run P4 was chosen to characterize penetrative convection conditions. All three curves are approximately linear in the mixed layer. This indicates that the moments involving temperature are steady state, even though the total kinetic energy evolves with time in runs N1 and N2.

Figure 14 shows the dimensionless mean temperature lapse rates for runs N1, N2, and P4. In addition, a curve obtained for a numerical simulation of nonpenetrative convection in a tank (Sorbjan 1996) is shown for comparison. A remarkable agreement of the considered statistic for the nonpenetrative tank and cases N1 and N2 is obtained up to about $0.8z_i$. The fact that

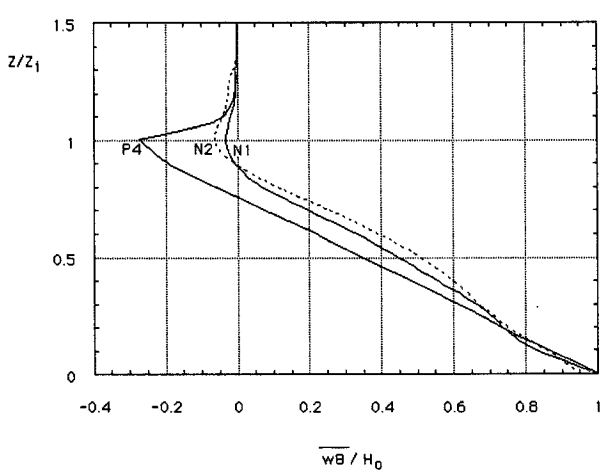


FIG. 13. Dimensionless virtual potential temperature heat flux for simulations N1, N2, and P4.

Unauthenticated | Downloaded 10/24/21 10:51 AM UTC

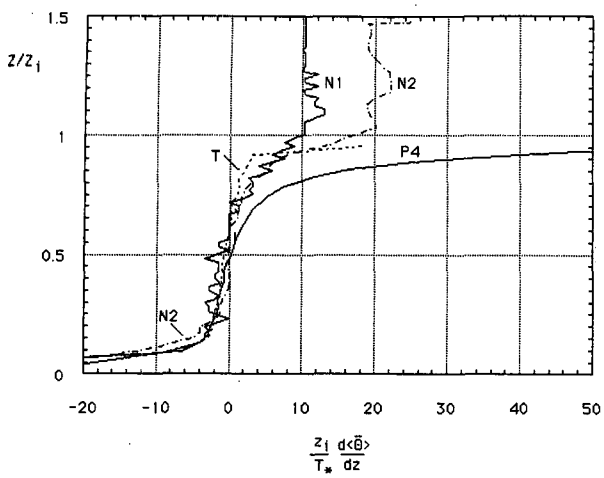


FIG. 14. Dimensionless virtual potential temperature lapse rate for simulations N1, N2, and P4. The curve obtained from solid-lid nonpenetrative simulation (Sorbjan 1996) is marked by letter "T."

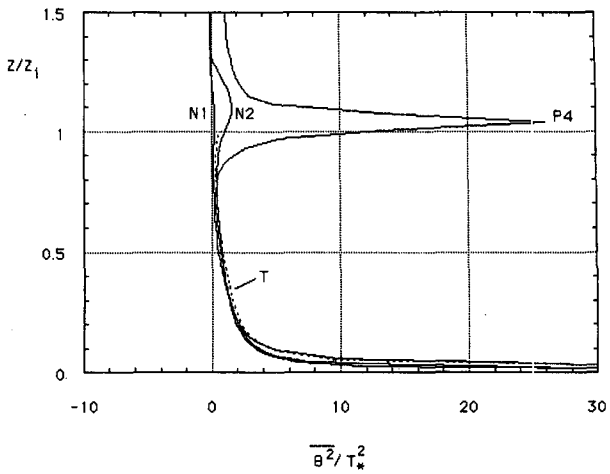


FIG. 15. Dimensionless virtual potential temperature variance for simulations N1, N2, and P4. The curve obtained from solid-lid nonpenetrative simulation (Sorbjan 1996) is marked by letter "T."

the curves in the figure from runs N1 and N2 (obtained at very different instants of time) coincide indicates that dimensionless temperature lapse rates do not evolve with time. Dimensionless temperature lapse rates obtained in solid-lid nonpenetrative convection (marked in the figure by letter T) and in runs N1 and N2 are nearly identical.

The dimensionless potential temperature variance is shown in Fig. 15. Also for this moment, an agreement is observed for the solid-lid case (marked in the figure by letter T) and runs N1 and N2. Curves N1 and N2 coincide despite significantly different lengths of both simulations.

Our results presented in Figs. 13 and 15 can be compared with the statistics obtained in a wind tunnel by Fedorovich et al. (1995). Values of the parameter $S = Nt^*$ in Fedorovich et al.'s experiments were in the range from 2 to 3, quite close to the values of $S$ in runs N1 and N2 in Table 1. In agreement with Fig. 14, the heat flux obtained in the wind tunnel linearly decreases to a low value of about $-0.05H_0$ at the top of the mixed layer. At the same time, the maximum value of the dimensionless potential temperature variance above the top of the mixed layer is about 0.5. This agrees with the variances in runs N1 and N2 shown in Fig. 15.

It should be noted that in the free-encroachment runs N1 and N2 there is a penetration of the nearly neutral capping layer by thermals generated near the heated surface. In run N1, the speed of rising updrafts at the top of the mixed layer is $w_i^{\uparrow} = 0.13w^*$. We should also recall the previously obtained result for run N1 that $dz_i/dt = 0.16w^*$. Both facts indicate that approximately $dz_i/dt \sim w_i^{\uparrow} \sim 0.15w^*$ (the value 0.15 is a compromise between constants 0.13 and 0.16), that is, that the top of the mixed layer $z_i$ is lifted upward with the speed of rising updrafts. Consequently, even though updrafts do penetrate the isothermal layer, there is no net penetration above the mixed layer height $z_i$. In this sense, the free-encroachment regime is nonpenetrative. As a result, its thermal structure is similar to the solid-lid nonpenetrative convection in a tank. It should be stressed that both regimes are similar only with respect to their thermal structure and that their dynamical structure differs.

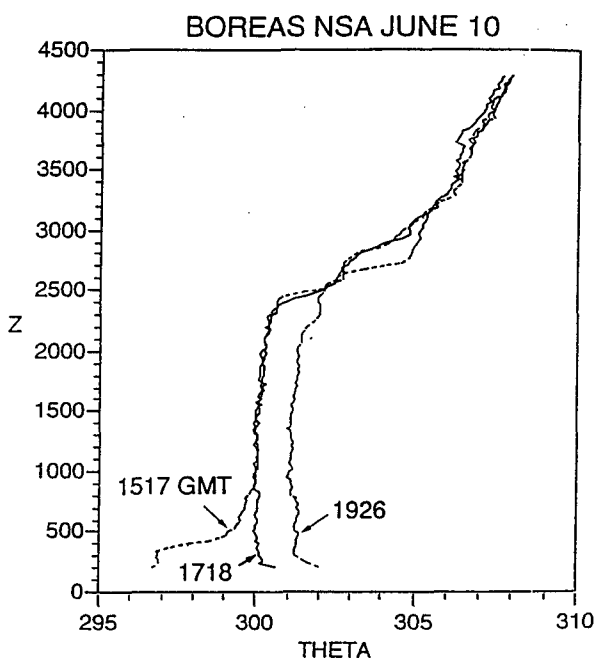


FIG. 16. Sounding of the potential temperature measured on 10 June 1994 during the BOREAS experiment at 1517, 1718, and 1926 UTC (GMT) (0917, 1118, and 1226 LT) (MacPhearson and Betts 1995).

Unauthenticated | Downloaded 10/24/21 10:51 AM UTC

As depicted in Fig. 16, free encroachment occurs when, above the surface nocturnal temperature inversion, there is a well-mixed layer left unchanged from the previous day. After sunrise, the surface potential temperature increases and eventually reaches the temperature in the elevated mixed layer. At this moment $\Gamma$ is nearly nil. The resulting regime lasts as long as it takes the updrafts to travel from the actual mixed height $z_{i1}$ to the top of the elevated mixed layer $z_{i2}$. Assuming that the mixed layer growth rate is about $0.15w^*$, we can estimate this time interval as $\tau \sim 7(z_{i2} - z_{i1})/w^*$. For the case in Fig. 16 we have $z_{i1} = 1000$ m and $z_{i1} = 2500$ m. Applying a formula obtained by Sorbjan (1995), $H_0 = 0.75 z_i \Delta\theta/\Delta t$, where $\Delta\theta$ is the time change of the potential temperature in the mixed layer during a time interval $\Delta t$, we can calculate (for the interval from 1718 to 1926 UTC) that $w^* \sim 3$ m s$^{-1}$, which yields $\tau \approx 1$ h.

## 5. Final remarks

In the presented paper here, a "large eddy simulation" model of the convective boundary layer was employed to examine effects caused by a variation of the temperature lapse rate $\Gamma$ in the free atmosphere. The obtained results showed that statistical moments involving only the vertical velocity are practically independent of $\Gamma$. Statistical moments involving temperature have two different regimes. The first regime covers the lower 90% portion of the mixed layer and is independent of $\Gamma$. The dimensionless statistics in this regime (such as temperature lapse rate, temperature variance, vertical transport of temperature variance, and vertical transport of temperature flux) are uniquely dependent on only one dimensionless parameter, $z/z_i$. The second regime is located near the top of the convective boundary layer. Deardorff's mixed layer similarity does not apply in this layer. Statistics of turbulence in this layer are strongly dependent on a parameter $\Gamma$.

The ratio $R$ of the heat fluxes at the top and the bottom of the mixed layer increases when $\Gamma$ increases. For the values of $\Gamma$ from 1 to 10 K/km, typically observed in the atmosphere, the heat flux ratio $R$ varies in the range $-0.2$ to $-0.3$. When $\Gamma$ increases by an order of magnitude to 100 K/km, $R$ increases only slightly to about $-0.4$. Statistical moments involving specific humidity are also strongly dependent on $\Gamma$. The humidity flux and the humidity variance decrease when $\Gamma$ increases.

Numerical experiments showed that a nonpenetrative regime with a zero heat flux at the top of the mixed layer cannot be induced by imposing a strong capping inversion with large $\Gamma$. A nil heat flux at the top of the mixed layer would occur only when $\Gamma$ vanished. Such a case can be called free encroachment and can be observed in the morning atmosphere when an elevated well-mixed layer left from the previous day, is extended down to the surface as a result of a warming of the underlying surface and erosion of the nocturnal surface inversion. The resulting regime lasts typically from a few minutes to an hour and eventually evolves into penetrative convection.

During free encroachment, updrafts penetrate the isothermal layer; nevertheless, there is no net penetration above the mixed layer height $z_i$, which is lifted upward with the speed of rising updrafts. In this sense, the free-encroachment regime is nonpenetrative. As a result, its thermal structure is similar to the solid-lid nonpenetrative convection in a tank.

*Acknowledgments.* This research was sponsored by NSF Grant ATM 9217028. The author would like to thank Dr. Richard Doviak for his comments.

REFERENCES

Adrian, R. J., R. T. S. Ferreira, and T. Boberg, 1986: Turbulent thermal convection in wide horizontal fluid layers. *Exp. Fluids,* **4,** 121–141.

Boers, R., 1989: A parameterization of the depth of the entrainment zone. *J. Appl. Meteor.,* **28,** 107–111.

Carson, D., and F. B. Smith, 1974: Thermodynamic model for the development of a convectively unstable boundary layer. *Advances in Geophysics,* Vol. 18A, Academic Press, 111–124.

Caughey, S. J., 1982: Observed characteristics of the atmospheric convective boundary layer. *Atmospheric Turbulence and Air Pollution Modelling,* F. T. Nieuwstadt and H. van Dop, Eds., Reidel, 107–158.

——, and S. G. Palmer, 1979: Some aspects of turbulence structure through the depth of the convective boundary layer. *Quart. J. Roy. Meteor. Soc.,* **105,** 811–827.

Deardorff, J. W., 1970a: Preliminary results from numerical integration of the unstable planetary boundary layers. *J. Atmos. Sci.,* **27,** 1209–1211.

——, 1970b: Convective velocity and temperature scales for the unstable planetary boundary layer and for Rayleigh convection. *J. Atmos. Sci.,* **27,** 1211–1212.

——, 1974a: Three-dimensional numerical study of the height and mean structure of a heated planetary boundary layer. *Bound.-Layer Meteor.,* **7,** 81–106.

——, 1974b: Three-dimensional numerical study of turbulence in an entraining mixed layer. *Bound.-Layer Meteor.,* **7,** 199–226.

——, 1976: On the entrainment rate of a stratocumulus-topped mixed layer. *Quart. J. Roy. Meteor. Soc.,* **102,** 563–582.

——, G. E. Willis, and D. K. Lilly, 1969: Laboratory investigation of non-steady penetrative convection. *J. Fluid Mech.,* **35,** 7–31.

——, ——, and B. H. Stockton, 1980: Laboratory studies of entrainment zone of a convectively mixed layer. *J. Fluid Mech.,* **100,** 41–64.

Fedorovich, E., R. Kaiser, and M. Rau, 1995: Simulation of convective boundary layer turbulence in the thermally stratified wind tunnel. Preprints, *11th Symp. on Boundary Layers and Turbulence,* Charlotte, NC, Amer. Meteor. Soc., 424–427.

Hartman, D. L., 1994: *Global Physical Climatology.* Academic Press, 410 pp.

Krettenauer, K., and U. Schumann, 1992: Numerical simulation of turbulent convection over wavy terrain. *J. Fluid Mech.,* **237,** 261–299.

Kumar, R., and R. J. Adrian, 1986: Higher order moments in the entrainment zone of turbulent penetrative thermal convection. *J. Heat Transfer,* **108,** 323–329.

Lilly, D. K., 1968: Models of cloud-capped mixed layers under a strong inversion. *Quart. J. Roy. Meteor. Soc.,* **94,** 292–309.

MacPhearson, L. I., and A. K. Betts, 1995: Aircraft encounters with strong coherent vorticies over the boreal forest. Preprints, *11th*

Unauthenticated | Downloaded 10/24/21 10:51 AM UTC

*Symp. on Boundary Layers and Turbulence,* Charlotte, NC, Amer. Meteor. Soc., 424–427.

Mahrt, L., 1979: Penetrative convection at the top of a growing boundary layer. *Quart. J. Roy. Meteor. Soc.,* **105,** 969–985.

Nieuwstadt, F. T. M., P. J. Mason, C.-H. Moeng, and U. Schumann, 1992: Large-eddy simulation of convective boundary-layer: A comparison of four computer codes. *Turbulent Shear Flows 8.* F. Durst, R. Friedrich, B. E. Launder, F. W. Schmidt, U. Schumann, and J. H. Whitelaw, Eds., Springer-Verlag, 343–367.

Rayment, R., and C. J. Readings, 1974: A case study of the structure and energetics of an inversion. *Quart. J. Roy. Meteor. Soc.,* **100,** 221–233.

Schmidt, H., and U. Schumann, 1989: Coherent structure of the convective boundary layer derived from large-eddy simulation. *J. Fluid. Mech.,* **200,** 511–562.

Schumann, U., 1991a: Subgrid length-scales for large-eddy simulation of stratified turbulence. *Theor. Comput. Fluid Dyn.,* **2,** 279–290.

——, 1991b: Simulations and parameterizations of large eddies in convective atmospheric boundary layers. *Workshop on Fine Scale Modelling and the Development of Parameterization Schemes,* Reading, England, European Centre for Medium-Range Weather Forecasts, 21–51.

——, and C.-H. Moeng, 1991: Plume fluxes in clear and cloudy convective boundary layers. *J. Atmos. Sci.,* **48,** 1746–1757.

Sorbjan, Z., 1990: Similarity scales and universal profiles of statistical moments in the convective boundary layer. *J. Appl. Meteor.,* **29,** 1565–1583.

——, 1995: Toward evaluation of heat fluxes in the convective boundary layer. *J. Appl. Meteor.,* **34,** 1092–1098.

——, 1996: Numerical study of penetrative and "solid lid" nonpenetrative convective boundary layers. *J. Atmos. Sci.,* **53,** 101–112.

Willis, G. E., and J. W. Deardorff, 1974: A laboratory model of the unstable planetary boundary layer. *J. Atmos. Sci.,* **31,** 1297–1307.

Wyngaard, J. C., 1985: Structure of the planetary boundary layer and implications for its modeling. *J. Climate Appl. Meteor.,* **24,** 1131–1142.

Young, G. S., 1988: Turbulence structure of the convective boundary layer. Part II: Phoenix 78 aircraft observations of thermals and their environment. *J. Atmos. Sci.,* **45,** 727–735.

Zeman, D., and H. Tennekes, 1977: Parameterization of the turbulent energy budget at the top of the daytime atmospheric boundary layer. *J. Atmos. Sci.,* **34,** 111–123.

Unauthenticated | Downloaded 10/24/21 10:51 AM UTC